

# Minkowski Functionals of SDSS galaxies I : Analysis of Excursion Sets

Chiaki HIKAGE<sup>1</sup>, Jens SCHMALZING<sup>2</sup>, Thomas BUCHERT<sup>1,2,3</sup>, Yasushi SUTO<sup>1</sup>,  
Issha KAYO<sup>1</sup>, Atsushi TARUYA<sup>1</sup>, Michael S. VOGLEY<sup>4</sup>, Fiona HOYLE<sup>4</sup>,  
J. Richard GOTT III<sup>5</sup>, Jon BRINKMANN<sup>6</sup>, et al.

<sup>1</sup>*Department of Physics, School of Science, University of Tokyo, Tokyo 113-0033*

<sup>2</sup>*Theoretische Physik, Ludwig-Maximilians-Universität,  
Theresienstr. 37, D-80333 München, Germany*

<sup>3</sup>*Research Center for the Early Universe (RESCEU), School of Science,  
University of Tokyo, Tokyo 113-0033*

<sup>4</sup>*Department of Physics, Drexel University, 3141 Chestnut Street, Philadelphia, PA 19104, USA*

<sup>5</sup>*Princeton University Observatory, Peyton Hall, Princeton, NJ 08544, USA*

<sup>6</sup>*Apache Point Observatory, P.O.Box 59, Sunspot NM 88349-0059, USA*

*hikage@utap.phys.s.u-tokyo.ac.jp, jens@theorie.physik.uni-muenchen.de,  
buchert@theorie.physik.uni-muenchen.de, suto@phys.s.u-tokyo.ac.jp,  
kayo@utap.phys.s.u-tokyo.ac.jp, ataruya@utap.phys.s.u-tokyo.ac.jp,  
vokeley@drexel.edu, hoyle@venus.physics.drexel.edu, jrg@astro.princeton.edu, jb@apo.nmsu.edu*

(Received 2003 April 9; accepted 2003)

## Abstract

We present a first morphometric investigation of a preliminary sample from the SDSS of 154287 galaxies with apparent magnitude  $14.5 < m_r < 17.5$  and redshift  $0.001 < z < 0.4$ . We measure the Minkowski Functionals, which are a complete set of morphological descriptors. To account for the complicated wedge-like geometry of the present survey data, we construct isodensity contour surfaces from the galaxy positions in redshift space and employ two complementary methods of computing the Minkowski Functionals. We find that the observed Minkowski Functionals for SDSS galaxies are consistent with the prediction of a  $\Lambda$ -dominated spatially-flat Cold Dark Matter model with random-Gaussian initial conditions, within the cosmic variance estimated from the corresponding mock catalogue. We expect that future releases of the SDSS survey will allow us to distinguish morphological differences in the galaxy distribution with regard to different morphological type and luminosity ranges.

**Key words:** cosmology: large-scale structure of universe — cosmology: observations — methods: statistical

## 1. Introduction

The first-year WMAP (*Wilkinson Microwave Anisotropy Probe*) data allow measurement of the parameters of the standard cosmological model to unprecedented accuracy; it now seems reasonable to assume  $\Omega_m \approx 0.3$ ,  $\Omega_\Lambda \approx 0.7$ , and  $h \approx 0.7$  (Spergel et al. 2003). Furthermore, the data put stringent constraints on non-Gaussian signatures in the primordial density fluctuations at  $z \approx 1000$  (Komatsu et al. 2003; Colley & Gott 2003). These results point to two important and complementary questions for cosmology in this century: origin and evolution. The former regards the question of how our universe came to have the observed values of the cosmological parameters including questions of their intrinsic nature. The latter question asks how the universe at  $z \approx 1000$  revealed by WMAP leads to the rich current structure traced by galaxies. The present study is an attempt to address the latter by characterizing and quantifying the morphological properties of the galaxy distribution of Sloan Digital Sky Survey (SDSS) spectroscopic catalogues through estimation of the Minkowski Functionals (Mecke et al. 1994; Schmalzing and Buchert 1997).

We have three primary goals for analyzing galaxy catalogues with Minkowski Functionals (hereafter MFs): the first is to test Gaussianity of the primordial density fluctuations. Indeed, tests of Gaussianity used to be of primary importance before the discovery of the CMB (Cosmic Microwave Background) temperature anisotropy, but now have been superseded by the CMB map analysis, although measurement of the MFs is still useful as an independent tool. The second goal is to understand the evolution of galaxy clustering, with particular emphasis on the morphology of large-scale structure. Since the primordial Gaussianity has been fairly well-established, studying the growth of structure should be the major role of the MFs, which complement estimation of the N-point correlation functions. Finally, we can examine whether the current observational catalogues may be regarded as fair samples of the density distribution in the Universe. In reality, however, those primary goals may be achieved barely partially with the current dataset that we use below. Nevertheless our results shown below should be regarded as the most careful attempt towards the goals on the basis of the best observational data currently available.

Focusing on morphological properties has two major advantages. First, there is a firm mathematical basis of morphological statistics developed in the field of integral geometry, which has condensed the complex information about morphology that is contained in all orders of the N-point correlation functions into a set of  $d + 1$  functionals, where  $d$  is the dimension of the spatial pattern (Mecke et al. 1994; Kerscher 2000 and references to the mathematical literature therein). Second, because this reduced set implicitly contains information from higher-order correlation functions, they provide constraints that are complementary to low-order correlation function analysis (e.g., Mecke et al. 1994, Schmalzing et al. 1999b). As a consequence of including higher-order correlation terms, the MFs also cover phase-correlations that are essential

for the formation of large-scale structure. In particular, the MFs are sensitive to features on spatial scales larger than typical scales ( $\approx 5h^{-1}\text{Mpc}$ ) accessible by the two-point correlation function, as demonstrated by Kerscher et al. 1998.

A spatial distribution in three dimensions has four Minkowski Functionals, namely its volume, its surface area, the integrated mean curvature and the integrated Gaussian curvature, i.e., the Euler characteristic. The latter measures the same property as the Genus (Gott et al. 1986, Melott 1988) which is a commonly used statistic in large-scale structure analysis. Using the whole family of MFs turns out to provide useful additional information: previous experience already demonstrated that the total surface area (*c.f.*, Ryden 1988; Ryden et al. 1989) and the integral mean curvature are more significant in discriminating structural differences. Furthermore, integral geometry provides robust formulae to deal with bounded data sets; in fact the boundary effect can only be exactly deconvolved by using the complete set of MFs (e.g., Kerscher et al. 1998). Useful ‘shapefinders’ can be constructed on the basis of isoperimetric ratios among the MFs (Sahni et al. 1998, Schmalzing et al. 1999a).

A natural method to evaluate the MFs of a point-distribution, such as a galaxy catalogue, is the so-called ‘Boolean Grain Model’, which decorates each point in the sample with, in the simplest case, spherical balls; the body formed by the union of these balls at a given scale (the radius of the balls) is then measured with MFs (Mecke et al. 1994). This method is usually preferable to the construction of a density field by smoothing and measurement of the morphology of isodensity contour surfaces, because the former has only one parameter (the radius) and does not require a smoothing kernel that discards information. However, the Boolean Grain Model has limitations when it comes to analyzing slice-like data such as the present sample of the SDSS data set: the largest Boolean Grain (sphere) is the one that fills the smallest extent of the sample and therefore the analysis is limited to that scale. For this reason we choose to smooth the point distribution with a Gaussian and construct excursion sets (isodensity contours) as a sensible way to study the morphology of large-scale structure in these data. Because the weak point in this analysis is the reliability of the constructed density field on a given smoothing scale, we employ two complementary methods of calculating the MFs of isodensity contour surfaces, which introduces a systematic control element into our analysis (Schmalzing and Buchert 1997).

This paper is organized as follows. In Section 2 we explain and illustrate the SDSS data set we analyze and describe the mock catalogues used for comparison. In Section 3 we introduce the Minkowski Functionals, especially the computational methods of their calculation (details are provided in Appendix A). In this section we investigate systematic problems of the analyzed sample such as boundary effect, spatial resolution, and smoothing scale. Section 4 is devoted to the analysis of volume-limited samples, while the corresponding results for the apparent-magnitude limited samples are discussed in Appendix B. Among other issues we address is the fair sample question, including a convergence study by comparing with a previous data set.

Finally, Section 5 is devoted to a summary of the results and further discussion.

## 2. SDSS Galaxy and N-body Mock Catalogues

### 2.1. SDSS Sample

York et al. (2000) provide an overview of the SDSS. Stoughton et al. (2002) describe the Early Data Release (EDR) and details about the measurements. Technical articles providing details of the SDSS include the description of the photometric camera (Gunn et al. 1998), photometric analysis (Lupton et al. 2002; Stoughton et al. 2002), the photometric system (Fukugita et al. 1996; Hogg et al. 2001; Smith et al. 2002), astrometric calibration (Pier et al. 2002), selection of the galaxy spectroscopic samples (Strauss et al. 2002; Eisenstein et al. 2001), and spectroscopic tiling (Blanton et al. 2002).

Our analysis of the MFs in the present paper is based on a subset of the SDSS galaxy redshift data, ‘Large-scale Structure Sample 12’ (Blanton et al. 2002). This sample includes galaxies with r-band magnitudes between 14.5 and 17.5 after correction for Galactic reddening using the maps of Schlegel, Finkbeiner, & Davis (1998).

A map of the galaxy distribution of the data that we analyze, together with a typical slice, are shown in Figures 1, 2 and 3. The three-dimensional map centered on us in equatorial coordinate system is shown in the upper panel of Figure 1. The lower panel in this figure shows the map projected onto the celestial sphere. The projected skymap for each Region is plotted in the survey coordinate system in Figure 2. Redshift slices of galaxies centered around the equatorial plane with various redshift limits and thicknesses of planes are shown in Figure 3:  $z < 0.05$  with thickness of  $10h^{-1}\text{Mpc}$  centered around the equatorial plane in the upper-left panel;  $z < 0.1$  with thickness of  $15h^{-1}\text{Mpc}$  in the upper-right panel;  $z < 0.2$  with thickness of  $20h^{-1}\text{Mpc}$  in the lower panel.

The data are mainly located in three regions, which we call Region 1, 2 and 3, respectively. The properties of each region covering the range of right ascension  $\alpha$  and declination  $\delta$  of the equatorial coordinate system, and the number of galaxies are listed in Table 1. SDSS photometry is taken in driftscan mode along great circles along arcs of constant  $\eta$  in the survey coordinate system  $(\lambda, \eta)$ . The survey coordinate system  $(\lambda, \eta)$  is suitable to describe the survey area, because each drift scan is perpendicular to a line of constant  $\mu$ . The transformation between celestial and survey coordinates is

$$\begin{aligned} \cos(\alpha - 95^\circ) \cos \delta &= -\sin \lambda \\ \sin(\alpha - 95^\circ) \cos \delta &= \cos \lambda \cos(\eta + 32.5^\circ) \\ \sin \delta &= \cos \lambda \sin(\eta + 32.5^\circ). \end{aligned} \tag{1}$$

In this paper we do not present the results of our analysis of the data located in Region 3 (Southern sky) containing the three  $2.5^\circ$  width consecutive stripes separated from each other.

The reason is that no additional information on the morphology of three-dimensional structure could be deduced from this set due to its slice-like geometry. We also do not use the data in the discrete area in Region 2 ( $22.8^\circ \leq \lambda \leq 36.1^\circ$ ,  $46.2^\circ \leq \eta \leq 51.3^\circ$ ) containing 3056 galaxies (Middle panel in Figure 2).

**Table 1.** Properties of three main regions of the SDSS ‘Sample 12’, including the range of each region in the equatorial coordinate system  $(\alpha, \delta)$  and the survey coordinate system  $(\lambda, \eta)$  (Eq.[1]).

Name	$\alpha$	$\delta$	$\lambda$	$\eta$	$N_{\text{gal}}$
Region 1	$129.7^\circ \sim 250.0^\circ$	$-3.74^\circ \sim 6.25^\circ$	$-55.2^\circ \sim 65.0$	$323.7^\circ \sim 333.8^\circ$	55897
Region 2	$112.0^\circ \sim 260.6^\circ$	$23.1^\circ \sim 68.8^\circ$	$-59.8^\circ \sim 60.4^\circ$	$16.2^\circ \sim 51.3^\circ$	59766
Region 3	$308.7^\circ \sim 63.3^\circ$	$-11.3^\circ \sim 16.3^\circ$	$-57.7^\circ \sim 55.8^\circ$	$130.6^\circ \sim 159.9^\circ$	38624

**Fig. 1.** *Upper:* 3D redshift-space map centered on us, and its projection on the celestial sphere of SDSS galaxy ‘Sample 12’, including the three main regions listed in Table 1. *Lower:* Projected skymap of ‘Sample 12’ galaxy data in equatorial coordinates  $(\alpha, \delta)$ .

**Fig. 2.** *Upper:* Projected skymap of ‘Sample 12’ galaxy data in the survey coordinate system  $(\lambda, \eta)$  in Region 1 (*Top*), Region 2 (*Middle*) and Region 3 (*Bottom*).

## 2.2. Mock samples

To test for several observational effects on the MFs, including the shape of the survey volume and the redshift distortion, we construct mock galaxy samples from a series of P<sup>3</sup>M  $N$ -body simulations provided by Jing and Suto (1998). These simulations employ  $256^3$  particles in a  $(300h^{-1}\text{Mpc})^3$  periodic comoving box using Gaussian initial conditions and a Cold Dark Matter (CDM) transfer function (Bardeen et al. 1986). We use the  $z = 0$  snapshot simulation data (for simplicity we neglect the light-cone effect) in two CDM cosmological models: Lambda-CDM (LCDM) with  $\Omega_0 = 0.3$ ,  $\lambda_0 = 0.7$ ,  $h = 0.7$ ,  $\Gamma = 0.21$ , and  $\sigma_8 = 1$ , and Standard-CDM (SCDM) with  $\Omega_0 = 1$ ,  $\lambda_0 = 0$ ,  $h = 0.5$ ,  $\Gamma = 0.5$ , and  $\sigma_8 = 0.6$ , where  $h$  denotes the Hubble constant in units of  $100\text{km s}^{-1}\text{Mpc}^{-1}$ ,  $\Gamma$  is the shape parameter of the transfer function, and  $\sigma_8$  is the r.m.s. density fluctuation amplitude at  $8h^{-1}\text{Mpc}$ . To simulate the effect of the shape of the survey volume, we extract wedge samples (12 realizations in total) out of the full simulation cube so that they have the same sample-shape and number of particles as each volume-limited sample. To construct mock samples that extend beyond the simulation box size, we duplicate particles using the periodic boundary conditions. We also consider the redshift distortion effect by adding the line-of-sight component of the peculiar-velocity to each particle in the calculation of the redshift.

**Fig. 3.** Redshift slices of ‘Sample 12’ galaxy data around the equatorial plane. The redshift limits and the thickness of the planes are: *Upper-left*  $z < 0.05$ ,  $10h^{-1}\text{Mpc}$ ; *Upper-right*  $z < 0.1$ ,  $15h^{-1}\text{Mpc}$ ; *Lower*  $z < 0.2$ ,  $20h^{-1}\text{Mpc}$ . The size of points has been adjusted. Note that the data for the Southern part are sparser than those for the Northern part, especially for thick slices (see Figure 1).

### 3. The Minkowski Functionals (MFs)

#### 3.1. Mathematical Aspects of Minkowski Functionals

The morphological properties of an  $n$ -dimensional pattern are completely described in terms of  $n + 1$  quantities, which we call MFs. In the present analysis, we generate isodensity contours from the three-dimensional density contrast field  $\delta$  by taking its excursion set  $F_\nu$ , i.e., the set of all points where the density contrast  $\delta$  exceeds the threshold level  $\nu$ . The four Minkowski Functionals  $V_k(\nu)$  of the excursion set can be measured, and plotted as functions of the threshold  $\nu$ . All MFs can be interpreted as well-known geometric quantities, namely the volume fraction  $V_0(\nu)$ , the total surface area  $V_1(\nu)$ , the integral mean curvature  $V_2(\nu)$ , and the integral Gaussian curvature, i.e., the Euler characteristic  $V_3(\nu)$ .

All MFs can be expressed as integrals over the excursion set. While the first MF is simply given by the volume integration of a Heaviside step function  $\Theta$  normalized to the total volume  $V_{\text{tot}}$ ,

$$V_0(\nu) = \frac{1}{V_{\text{tot}}} \int_V d^3x \Theta(\nu - \nu(x)), \quad (2)$$

the other MFs,  $V_k(k = 1, 2, 3)$ , are calculated by the surface integration of the local MFs,  $v_k^{\text{loc}}$  (Schneider 1978). The general expression is

$$V_k(\nu) = \frac{1}{V_{\text{tot}}} \int_{\partial F_\nu} d^2S(\mathbf{x}) v_k^{\text{loc}}(\nu, \mathbf{x}), \quad (3)$$

with the local Minkowski Functionals for  $k = 1, 2, 3$  given by

$$v_1^{\text{loc}}(\nu, \mathbf{x}) = \frac{1}{6}, \quad (4)$$

$$v_2^{\text{loc}}(\nu, \mathbf{x}) = \frac{1}{6\pi} \left( \frac{1}{R_1} + \frac{1}{R_2} \right), \quad (5)$$

$$v_3^{\text{loc}}(\nu, \mathbf{x}) = \frac{1}{4\pi} \frac{1}{R_1 R_2}, \quad (6)$$

where  $R_1$  and  $R_2$  are the principal radii of curvature of the isodensity surface.

For a 3-D Gaussian random field, the average MFs per unit volume can be expressed analytically as follows (Tomita 1990):

$$V_0(\nu) = \frac{1}{2} - \frac{1}{\sqrt{2\pi}} \int_0^\nu \exp\left(-\frac{x^2}{2}\right) dx, \quad (7)$$

$$V_1(\nu) = \frac{2}{3} \frac{\lambda}{\sqrt{2\pi}} \exp\left(-\frac{1}{2}\nu^2\right) \quad (8)$$

$$V_2(\nu) = \frac{2}{3} \frac{\lambda^2}{\sqrt{2\pi}} \nu \exp\left(-\frac{1}{2}\nu^2\right), \quad (9)$$

$$V_3(\nu) = \frac{\lambda^3}{\sqrt{2\pi}} (\nu^2 - 1) \exp\left(-\frac{1}{2}\nu^2\right), \quad (10)$$

where  $\lambda = \sqrt{\sigma_1^2/6\pi\sigma^2}$ ,  $\sigma \equiv \langle \delta^2 \rangle^{1/2}$ ,  $\sigma_1 \equiv \langle |\nabla\delta|^2 \rangle^{1/2}$ , and  $\delta$  is the density contrast.

In this paper we evaluate the MFs as a function of the threshold level. We employ two different definitions of this threshold: one is the density threshold level denoted by  $\nu_\sigma$ , which is given by the density contrast  $\delta$  divided by the r.m.s. density fluctuation  $\sigma$  after smoothing, the other is labeled by  $\nu_f$  parameterizing the volume-fraction  $f$  (Gott et al. 1986),

$$f = \frac{1}{\sqrt{2\pi}} \int_{\nu_f}^{\infty} e^{-x^2/2} dx. \quad (11)$$

The meaning of each definition is discussed in the section of the results for the MFs with volume-limited samples (§4).

### 3.2. Computational Methods

We compute the MFs for density contrast fields from mock samples and SDSS galaxies. We use the cloud-in-cell (CIC) interpolation to assign survey galaxies and dark matter particles to densities defined on a  $128 \times 256 \times 64$  grid. We Fourier transform the density contrast field, multiply by the Fourier transform of a Gaussian window with smoothing scale  $R_G$ ,

$$W_G(r) = \frac{1}{\sqrt{2\pi}R_G} \exp\left(-\frac{r^2}{2R_G^2}\right), \quad (12)$$

and then transform back to real space.

The accuracy of the estimation of the MFs increases in a specific volume as we choose smaller values of  $R_G$ , because the amplitudes of the MFs are roughly proportional to the number of structures with typical scale  $R_G$ . On the other hand, in order to produce reliable results of the MFs,  $R_G$  should be bounded by a minimum value for each sample to satisfy the following criteria (Hoyle et al. 2002):

1.  $R_G$  should be comparable to or larger than the mean separation of galaxies (using too small values of  $R_G$  reduces to spherical isodensity contours around each galaxy.)
2. The r.m.s. density fluctuation at the smoothing scale of  $R_G$  should be larger than the Poisson term, which is equal to the inverse square root of the galaxy number within a Gaussian ball of effective radius  $R_G$ .
3.  $R_G$  should be more than twice the mesh size, corresponding to the Nyquist resolution frequency.

A useful way to check for systematic errors due to numerical approximations inherent to each numerical code as well as due to the influence of the survey boundary is to compare the results with another code based on a different computational method. There are several

interesting routines to estimate the MFs, (e.g., Sheth et al. 2003), however, we here use two well-studied complementary routines to compute the MFs of a grid density field.

The first approach transforms the surface integrals in Equations (3) into volume integrals. The local Minkowski Functionals are expressed in terms of invariants formed from the first and second derivatives of the density contrast field (*cf.* Schmalzing & Buchert 1997 for an outline of this approach and Koenderink 1984, and Appendix A for the gory details). Hereafter we call this approach *Koenderink invariants*.

The other routine is based on Crofton’s formula (Crofton 1868) from integral geometry (Hadwiger 1957). A more detailed description of the method can be found in Schmalzing & Buchert 1997. This method, which we will refer to as *Crofton’s formula*, is best suited for a pattern described as a set of empty and occupied cells of a cubic grid. The calculation of Minkowski Functionals then reduces to counting the elementary cells (in three dimensions, the points, lines, squares, and cells of the cubic lattice), that are occupied by the pattern.

For the computation of the fourth MF  $V_3$ , we also apply the CONTOUR 3D code (Weinberg 1988), which has been widely used to calculate the genus  $g = -V_3$  (e.g., Gott et al. 1989). This code computes the integrated Gaussian curvature over the surface by considering the dataset to consist of cubic pixels, so the contour surface consists of faces, edges and vertices, and where all the curvature is concentrated at the vertices. The curvature integral is then calculated by summing the angle deficits (and subtracting the angle excesses) at the vertices.

Although the above three methods are theoretically equivalent, the numerical results are not always the same. This is partly due to the finite cell size of the grid used for our computations. However, the main difference comes from the effect of the complicated shape of the survey boundaries. In the following analysis we test the effect of excluding part of the volume near the boundary from our analysis, to find the limited spatial region in which the results from all three methods are consistent with each other.

### 3.3. Log-normal model as a standard of reference

The genus for the distribution of dark matter in simulations has been found to be well-approximated by the log-normal model (Matsubara and Yokoyama 1996; Hikage et al. 2002). Therefore, we might expect that this model would provide a reasonable approximation to all of the MFs of the dark matter distribution. Matsubara and Yokoyama (1996) derived the genus expression assuming that the nonlinear density field of dark matter has a one-to-one correspondence to the primordial Gaussian field. Generalizing their formula for the genus, the expressions for MFs that obey the log-normal statistics are obtained by substituting  $\nu_{\text{LN}}$  and  $\lambda_{\text{LN}}$  for  $\nu_\sigma$  and  $\lambda$  in Equations (7) to (10):

$$\nu_{\text{LN}}(\nu_\sigma) \equiv \frac{\ln[(1 + \nu_\sigma \sigma)\sqrt{1 + \sigma^2}]}{\sqrt{\ln(1 + \sigma^2)}}, \quad (13)$$

$$\lambda_{\text{LN}} \equiv \left( \frac{\sigma}{1 + \sigma^2 \log(1 + \sigma^2)} \right)^{1/2} \lambda. \quad (14)$$

Figure 4 shows the comparison between the log-normal model and the MFs of mock simulations estimated from both the Koenderink invariants and Crofton’s formula methods at  $R_G = 3, 7, 20h^{-1}\text{Mpc}$ . All of MFs except for  $V_0$  are multiplied by the volume of a Gaussian ball at the radius of  $R_G$ ,  $4/3\pi R_G^3$ . The error bar represents the statistical error estimated from three realizations of the full simulation. We find that all MFs obtained with the two methods agree very well over a wide range of smoothing scales. The log-normal model nicely reproduces all of the four MFs for dark matter and thus the difference between the log-normal model and the MFs for dark matter is negligible in the analysis of our galaxy samples with  $10^2 \sim 10^3$  times smaller volume (see Table 2) than that of the full cubic data.

## 4. Analysis of Volume-limited Samples

### 4.1. Construction of Volume-limited Samples

In an apparent-magnitude limited catalogue of galaxies, the average number density of galaxies decreases with distance because only increasingly bright galaxies are included in the sample at larger distance. To avoid this systematic change in both density and galaxy luminosity we construct volume-limited samples of galaxies, with cuts on both absolute-magnitude and redshift (we do not attempt to correct for evolution in the galaxy population over these limited ranges of redshift). In this section we mainly study the dependencies on galaxy luminosity and morphological type of the MFs for the volume-limited samples, and compare with the corresponding mock catalogues. We construct six volume-limited samples in Region 1 and Region 2 covering ranges of absolute magnitude of width  $\Delta M_r = 1$  from  $-23$  to  $-17$ , where the absolute magnitude is

$$M_r = m_r - 5 \log[r(1+z)] + K(z), \quad (15)$$

and where  $K(z)$  is the K-correction for the bandpass shift due to the redshift. We apply an approximate K-correction factor  $K(z) = 0.9z$  valid for the typical galaxy color of  $g - r = 0.65$  (Fukugita et al. 1995). The maximum (minimum) redshift is determined by the redshift at which the faintest (brightest) galaxies in each sample lies in the apparent-magnitude range  $14.5 < m_r < 17.5$  (see Figure 5). The bright cutoff in this apparent magnitude range approximates the three arcsecond aperture magnitude limit in the spectroscopic target selection (see Strauss et al. 2002 for details). We compute the comoving distance from the observed redshift  $z$  of each galaxy after correction for the Local Group motion,

$$d_c(z) = \int_0^z \frac{dz'}{\sqrt{\Omega_0(1+z')^3 + (1 - \Omega_0 - \lambda_0)(1+z')^2 + \lambda_0}}, \quad (16)$$

where  $\Omega_0$  is the matter density parameter and  $\lambda_0$  is the dimensionless cosmological constant. Table 2 shows the redshift range and the total volume of each volume-limited sample.

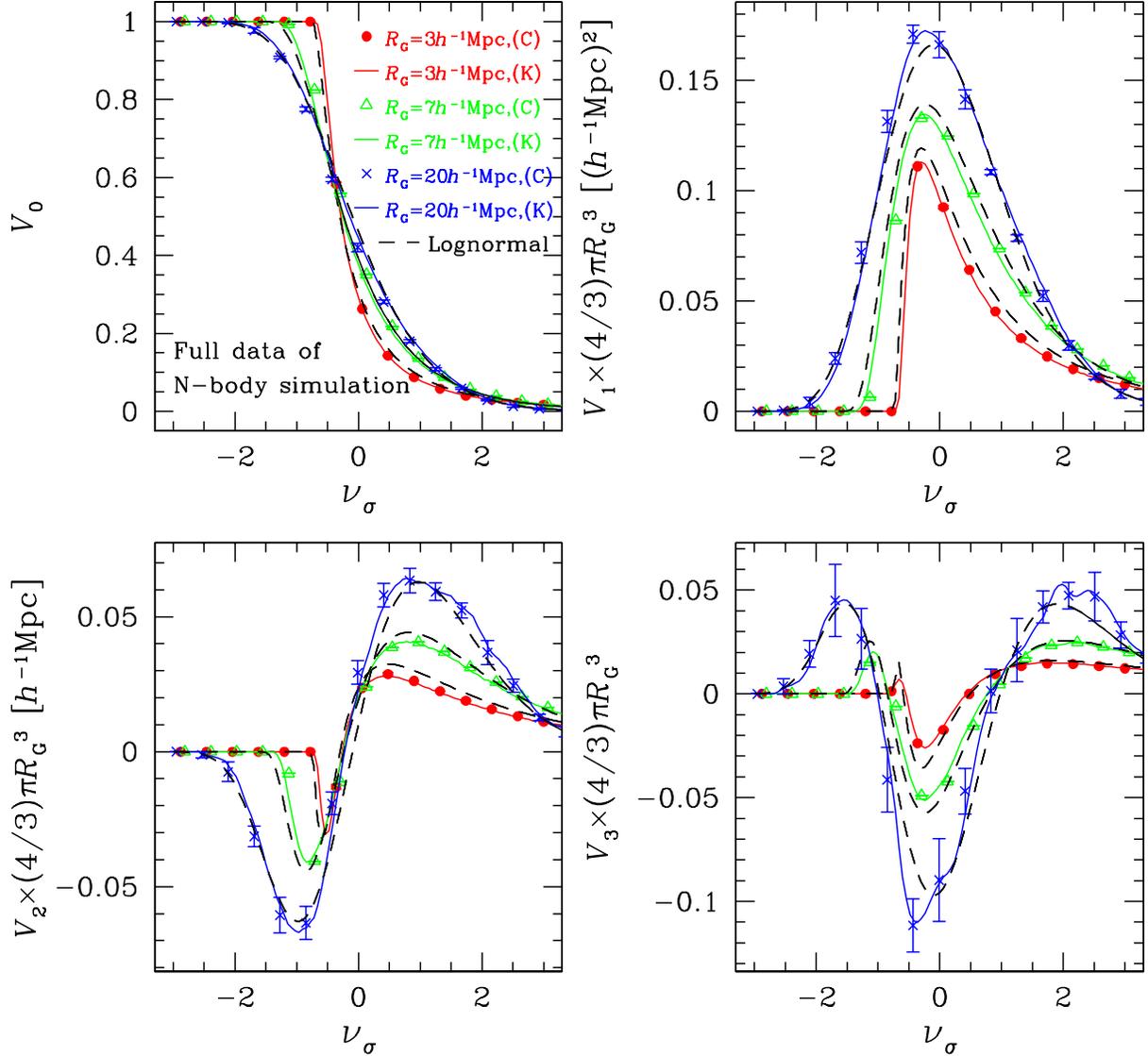


**Fig. 4.** Comparison of the MFs for dark matter using all particles in N-body simulations ( $(300h^{-1}\text{Mpc})^3$ ) run by Jing & Suto (1998) with predictions of the log-normal model. Here we show estimates of the MFs using two methods: Crofton’s formula labeled by (C) at  $R_G = 3h^{-1}\text{Mpc}$  (filled circles),  $7h^{-1}\text{Mpc}$  (open triangles), and  $20h^{-1}\text{Mpc}$  (crosses), and the Koenderink invariants labeled by (K) at each smoothing scale (solid lines). The log-normal model predictions (Eq: (13)) are plotted with dashed lines at each smoothing scale. All of MFs except for  $V_0$  are multiplied by the volume of a Gaussian ball at the radius of  $R_G$ ,  $4/3\pi R_G^3$ . Error bars estimated from three realizations of cubic data are shown on the results from Crofton’s formula.

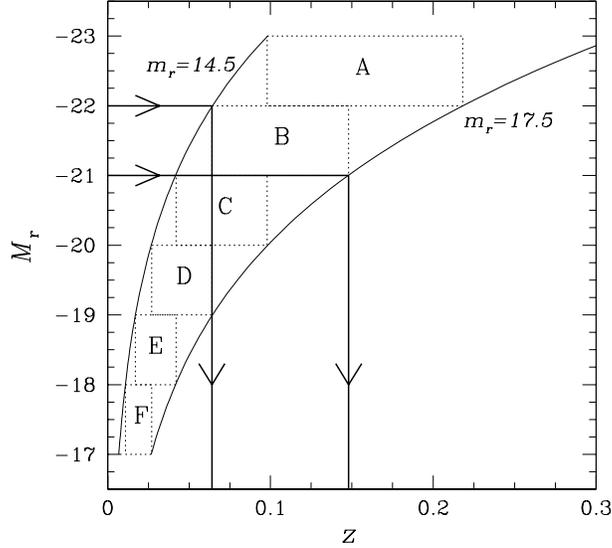


**Fig. 5.** Schematic picture to show how we determine the redshift range of a volume-limited sample with a given absolute-magnitude range. Six boxes represent the absolute-magnitude ranges and the redshift ranges of volume-limited samples listed in Table 2. Solid lines indicate the relation between  $M_r$  and  $z$  (Eq. (15)) at apparent magnitudes  $m_r = 14.5$  and  $17.5$ .

**Table 2.** Redshift range and survey volume in Regions 1 and 2 for each volume limited-sample with different magnitude ranges.

sample name	magnitude range	redshift range	total volume $[(h^{-1}\text{Mpc})^3]$	
			Region 1	Region 2
A	$-23 < M_r < -22$	$0.098 < z < 0.218$	$1.62 \times 10^7$	$1.86 \times 10^7$
B	$-22 < M_r < -21$	$0.064 < z < 0.148$	$5.40 \times 10^6$	$6.17 \times 10^6$
C	$-21 < M_r < -20$	$0.042 < z < 0.098$	$1.66 \times 10^6$	$1.90 \times 10^6$
D	$-20 < M_r < -19$	$0.027 < z < 0.064$	$4.81 \times 10^5$	$5.50 \times 10^5$
E	$-19 < M_r < -18$	$0.017 < z < 0.042$	$1.33 \times 10^5$	$1.52 \times 10^5$
F	$-18 < M_r < -17$	$0.011 < z < 0.027$	$3.57 \times 10^4$	$4.08 \times 10^4$

These galaxies are further classified into two morphological types, *Early-type* and *Late-type*, which basically correspond to E/S0 and Sp/Irr, respectively. Shimasaku et al. (2001) found a tight correlation between the morphology and the inverse concentration index  $c_{\text{in}}$ , defined as the ratio of the half-light Petrosian radius to the 90 %-light Petrosian radius (Stoughton et al. 2002). We adopt the threshold values of  $c_{\text{in}} = 0.35$  for  $m_r < 16.0$ ,  $0.359$  for  $16.0 < m_r < 16.5$ , and  $0.372$  for  $16.5 < m_r < 17.0$ . Since the discrimination of morphology is very difficult for  $m_r > 17.0$ , we count such faint galaxies neither as Early-type nor Late-type (this is why the number of galaxies for early and late types is different from that of all galaxies in Table 3). Table 3 shows the properties of each volume-limited sample including the numbers and the mean sep-

**Table 3.** Properties of volume-limited samples with different absolute-magnitude range, including the number of galaxies and the mean separation for All, Early-type and Late-type galaxies, respectively.

sample name	galaxy type	number of galaxies		mean separation [ $h^{-1}$ Mpc]	
		Region 1	Region 2	Region 1	Region 2
A	All	853	907	26.7	27.4
	Early	592	645	30.1	30.7
	Late	151	131	47.5	52.2
B	All	6727	6286	9.3	9.9
	Early	3570	3221	11.5	12.4
	Late	1938	1699	14.1	15.4
C	All	9783	7750	5.5	6.3
	Early	4049	3178	7.4	8.4
	Late	3849	3276	7.6	8.3
D	All	3677	4844	5.1	4.8
	Early	987	1256	7.9	7.6
	Late	2099	2644	6.1	5.9
E	All	1648	1671	4.3	4.5
	Early	245	253	8.2	8.4
	Late	1071	1073	5.0	5.2
F	All	686	416	3.7	4.6
	Early	63	37	8.3	10.3
	Late	422	258	4.4	5.4

arations for Early-type, Late-type and All (including the faint galaxies with  $17.0 < m_r < 17.5$ ) in each region.

Following the criteria for the smoothing scale  $R_G$  discussed above, we choose the three appropriate volume-limited samples and analyze them with smoothing lengths  $R_G = 3, 5, 7$  and  $10h^{-1}$ Mpc, respectively, listed in Table 4. The amplitude of the the MFs for each smoothed density field varies with the effective number of resolution elements in the sample  $N_{\text{res}}$  (Vogeley et al. 1994):

$$N_{\text{res}} = V_{\text{tot}} / (2\pi)^{3/2} R_G^3, \quad (17)$$

where  $V_{\text{tot}}$  is the total survey volume in which we compute the MFs. The estimator  $N_{\text{res}}$  indicates the number of structures at a typical scale  $R_G$  in the smoothed field and is roughly proportional to the amplitude of the MFs (the sampling noise of the MFs is roughly proportional to the inverse square root of  $N_{\text{res}}$ ). We also list the value of  $N_{\text{res}}$  for each smoothed density field in Table 4.

We calculate the r.m.s. fluctuation amplitude  $\sigma$  for each smoothed density field. Table

**Table 4.** Properties of density fields for each volume-limited sample including the smoothing scale  $R_G$ , the absolute-magnitude range, the mesh size of the simulation box, the resolution number  $N_{\text{res}}$  (Eq. (17)), and the r.m.s. density fluctuation amplitude  $\sigma$  of the SDSS galaxy number density field and the averaged  $\sigma$  with one-sigma error of the particle number density field in the mock samples.

$R_G$	sample name	mesh size	$N_{\text{res}}$		$\sigma$ of SDSS galaxies		$\sigma$ of mock samples	
			Region 1	Region 2	Region 1	Region 2	Region 1	Region 2
$3h^{-1}$ Mpc	D	$1.7 h^{-1}\text{Mpc}$	1131	1294	1.46	1.37	$1.38 \pm 0.06$	$1.38 \pm 0.13$
	E	$1.1 h^{-1}\text{Mpc}$	312	357	1.31	1.26	$1.28 \pm 0.13$	$1.38 \pm 0.16$
	F	$0.7h^{-1}$ Mpc	83	95	1.11	1.23	$1.47 \pm 0.54$	$1.68 \pm 0.58$
$5h^{-1}$ Mpc	C	$2.6 h^{-1}\text{Mpc}$	843	965	1.13	1.10	$0.94 \pm 0.03$	$1.00 \pm 0.07$
	D	$1.7 h^{-1}\text{Mpc}$	244	279	1.02	0.96	$0.94 \pm 0.04$	$0.95 \pm 0.09$
	E	$1.1 h^{-1}\text{Mpc}$	67	77	0.91	0.88	$0.89 \pm 0.10$	$0.94 \pm 0.10$
$7h^{-1}$ Mpc	C	$2.6 h^{-1}\text{Mpc}$	307	351	0.93	0.86	$0.72 \pm 0.03$	$0.77 \pm 0.05$
	D	$1.7 h^{-1}\text{Mpc}$	89	101	0.77	0.73	$0.70 \pm 0.04$	$0.73 \pm 0.07$
	E	$1.1 h^{-1}\text{Mpc}$	24	28	0.71	0.69	$0.70 \pm 0.10$	$0.71 \pm 0.07$
$10h^{-1}$ Mpc	B	$3.8 h^{-1}\text{Mpc}$	342	391	0.69	0.77	$0.58 \pm 0.02$	$0.62 \pm 0.03$
	C	$2.6 h^{-1}\text{Mpc}$	105	120	0.74	0.64	$0.53 \pm 0.02$	$0.58 \pm 0.04$
	D	$1.7 h^{-1}\text{Mpc}$	30	34	0.56	0.53	$0.51 \pm 0.04$	$0.54 \pm 0.06$

4 shows that  $\sigma$  of the SDSS galaxies agrees well with that of the dark matter samples within the standard deviation for all smoothing scales and samples with different magnitude ranges. This implies that the current data of SDSS galaxies may already approach a fair sample with respect to two-point measures on scales  $\leq 10h^{-1}\text{Mpc}$ . We also find that luminous galaxies exhibit stronger clustering (larger  $\sigma$ ).

**Fig. 6.** *top:* Illustration of a volume-limited sample C. Upper figures are redshift slice diagrams of Early-type (red), Late-type (blue), and Faint ( $17.0 < m_r < 17.5$ ) galaxies (black) for Region 1 (*left*) and Region 2 (*right*). Lower panels show redshift-space maps of the smoothed density field of the volume-limited sample for All, Early-type and Late-type galaxies at  $R_G = 7h^{-1}\text{Mpc}$ .

Figure 6 shows projected point distributions and contour plots of the density fields of the volume-limited samples smoothed at  $R_G = 7h^{-1}\text{Mpc}$  for Early-type, Late-type, and All galaxies, respectively (see discussion in Subsection 4.4).

Differences between estimates of the MFs using Crofton’s formula and the Koenderink invariants methods is shown in Figure 7. The methods yield consistent results except for  $V_2$ . In that case the difference is minimized to an acceptable level by restricting the region of analysis to a minimum of two grid cells from the boundary.

Here, two comments are in order: first,  $V_2$  is, according to many previous studies, the

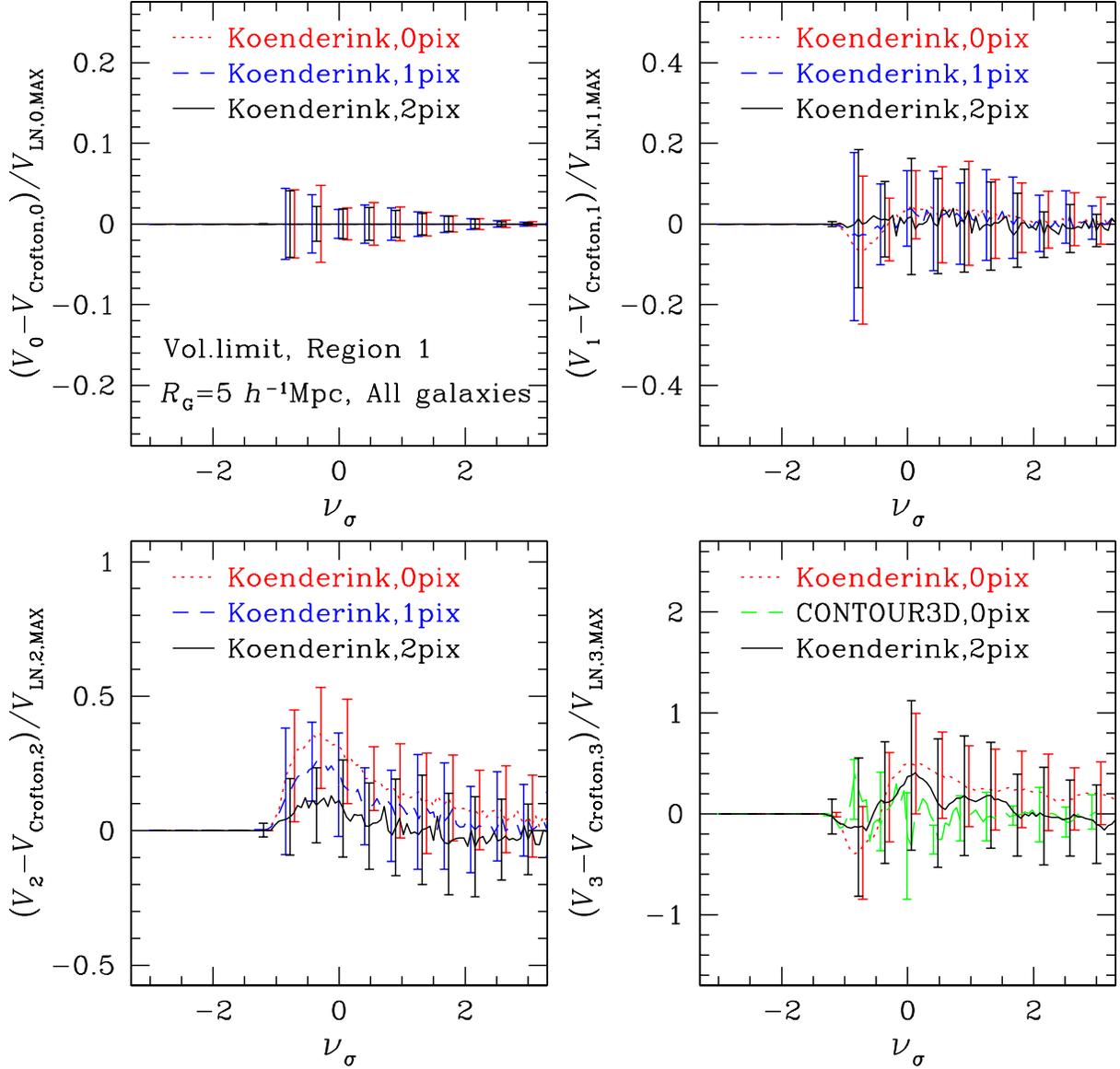


**Fig. 7.** Comparison of the two methods used to compute the MFs of mock volume-limited samples of Region 1. The plotted lines show the difference between the MF estimated using the Koenderink invariants method and the Crofton’s formula method, normalized by the MF amplitude predicted by the log-normal model. Error bars indicate the standard deviation estimated from the mock samples. The region near the survey boundary that is excluded from the analysis varies from zero (dotted lines), to one grid cell (dashed lines) or two grid cells (solid lines) from the survey edge. For the fourth MF,  $V_3(\nu_\sigma)$ , the difference between results from the CONTOUR 3D code (Weinberg 1998) and Crofton’s formula is plotted with dashed lines. The smoothing scale is  $R_G = 5h^{-1}\text{Mpc}$ , and the absolute-magnitude range is  $-20 < M_r < -19$ .

most sensitive of the four MFs to the morphology of large-scale structure. When the survey of the north galactic cap is completed,  $V_2$  will be accurately measured. Second, we found that the agreement between both methods is better for all MFs at smaller smoothing lengths. For  $V_3(\nu)$ , which is the same as the genus except for the sign, we also plot the difference between the Crofton’s formula results and the genus calculated by CONTOUR 3D (Weinberg 1998). The agreement between the two methods is also satisfactory. Therefore, we show only the estimation of the MFs based on Crofton’s formula for all MFs in what follows. In order to effectively enlarge the analyzed sample region and so improve on the significance of the results, we averaged the values for the MFs for Region 1 and Region 2. In doing so, we also take into account cosmic variance, to which we devote a separate study in the next subsection.

#### 4.2. Cosmic Variance

To examine whether Region 1 and Region 2 are fair samples for the purpose of measuring the MFs, we plot the difference between the observed MFs,  $V_{\text{obs},k}$ , and MFs from mock samples  $V_{\text{mock},k}$  for Region 1 and Region 2 simultaneously in Figure 8. We normalize the difference by the  $V_{\text{LN},1}(\nu)$ , which is the second MF predicted by the log-normal model (Eq. (13)) to remove the exponential damping nature of the MFs for large thresholds. The error bars on the line indicate the statistical error estimated from 12 realizations of the mock samples for each region.

We also compare the results for ‘Sample 12’ (lower panel in Figure 8) with the results of the previous ‘Sample 10’ (upper panel) which contains  $\sim 30\%$  fewer galaxies and has  $\sim 20\%$  smaller survey volume than ‘Sample 12’. We find that all of the four MFs marginally agree within the statistical error between Region 1 and Region 2 for ‘Sample 12’, while significant morphological fluctuations are seen in the MFs for Regions 1 and 2 of ‘Sample 10’.

This “convergence property” of our results by moving from ‘Sample 10’ to ‘Sample 12’ supports our methods of analysis and indicates that we obtained statistically reliable results. In the case of ‘Sample 12’ the variation of the MFs between Regions 1 and 2 is consistent with the uncertainties due to cosmic variance estimated using the mock samples. However, ‘Sample 10’ still displays significant morphological discrepancies. As we learned from previous studies of the PSCz catalogue (Kerscher et al. 2001) compared with the IRAS 1.2 Jy catalogue (Kerscher et al. 1998; 1997), morphological fluctuations on these spatial scales can be large, and the ‘fair sample scale’ may well be larger than  $300h^{-1}\text{Mpc}$ . Our previous studies mentioned above also showed that the sample-to-sample variation in mock catalogues critically depends on the size of the simulation box; simulations with box-size of the mock catalogues we employed in the present investigation are not expected to be able to reproduce the large morphological fluctuations that could be present on the scales considered. In any case, this is one of the critical issues that can be answered more reliably with the future samples of SDSS galaxies.

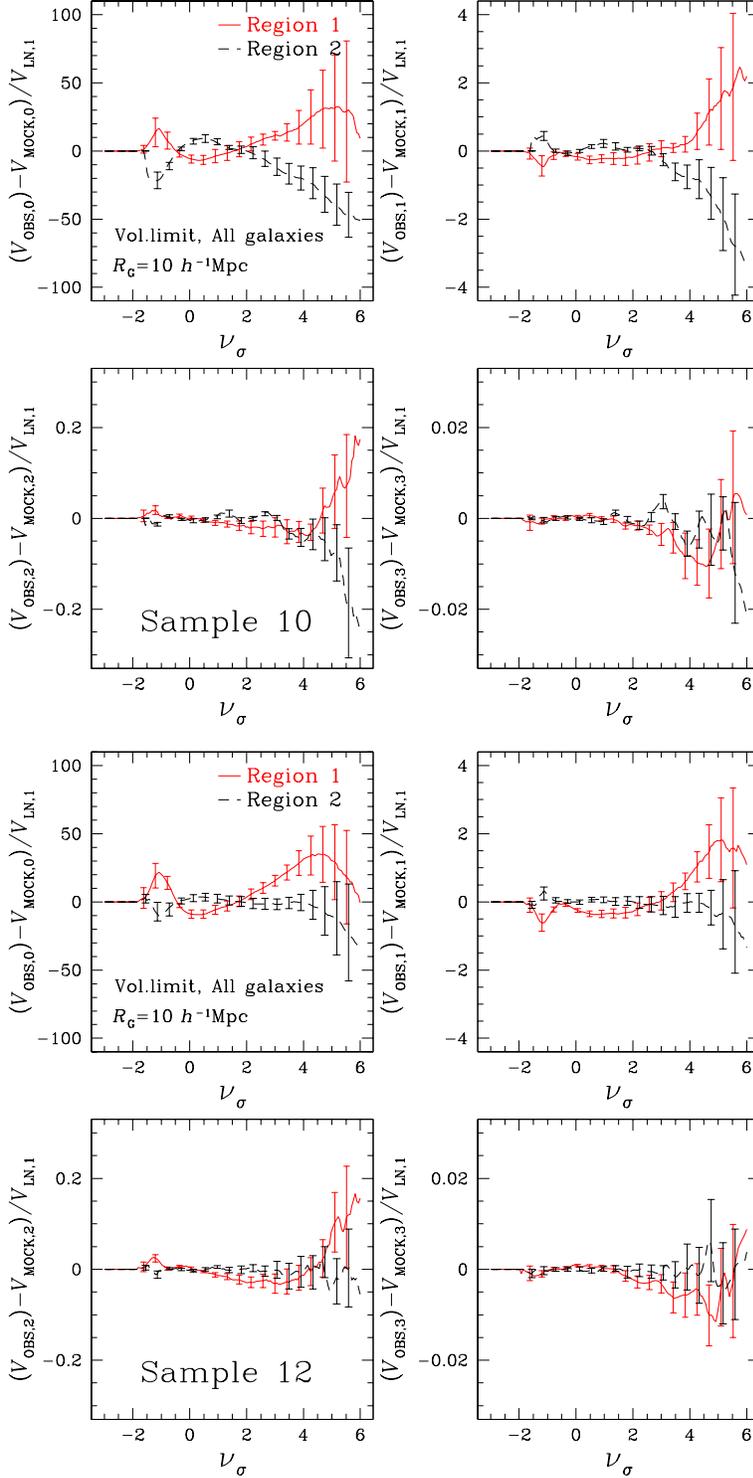


**Fig. 8.** Comparison of the MFs for the volume-limited samples of SDSS galaxies, Region 1 (solid lines) and Region 2 (dashed lines). We plot the difference between the MFs of the observations and mock surveys of each region, normalized by the amplitude of each MF predicted from the log-normal model for ‘Sample 10’ (upper panel) and ‘Sample 12’ (lower panel). Error bars indicate the standard deviation estimated from the mock results. The smoothing scale is  $R_G = 10h^{-1}\text{Mpc}$ , and the absolute-magnitude range is  $-20 < M_r < -19$ .

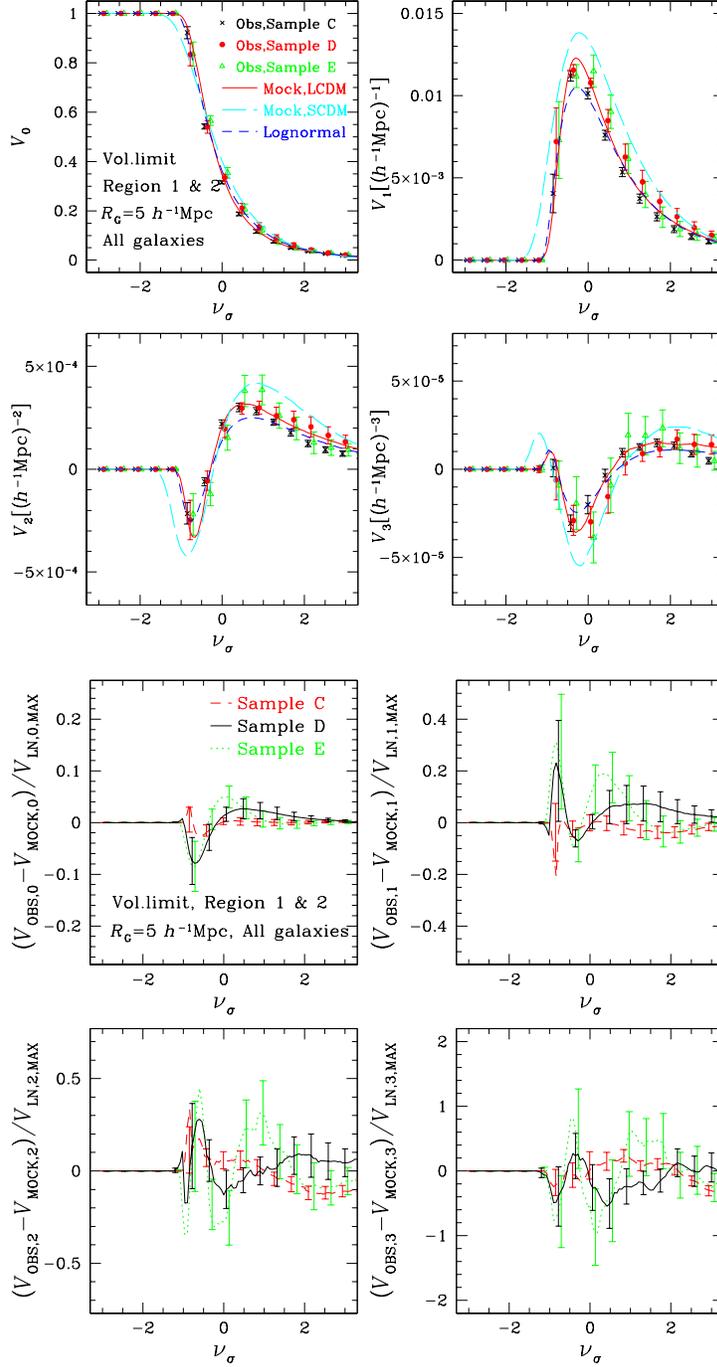


**Fig. 9.** Comparison of the MFs of volume-limited samples with different absolute-magnitude ranges (open triangles, filled circles and crosses in decreasing orders of  $M_r$ ). In the right set of panels, the lines represent the difference between the observed MFs and results for the mock samples from simulations, normalized by the amplitude of each MF predicted from the log-normal model. Sampling errors estimated from mock samples are plotted with the observational results. Averaged MFs of the mock samples are plotted for LCDM (solid lines) and SCDM (long dashed lines). Log-normal model predictions are also plotted with short dashed lines. Plotted lines are the average between Region 1 and 2 at  $R_C = 5h^{-1}\text{Mpc}$ .

### 4.3. Luminosity Segregation

In Figure 9 we plot the four MFs for the volume-limited samples at  $R_G = 5h^{-1}\text{Mpc}$  with three different absolute-magnitude ranges,  $-21 < M_r < -20$  (Sample C),  $-20 < M_r < -19$  (Sample D), and  $-19 < M_r < -18$  (Sample E) for Region 1 and 2 together. The properties of each volume-limited sample are listed in Table 4. The error bars on each observed MF represent the standard deviation estimated from the mock samples. For comparison we plot the averaged MFs for the mock samples with intermediate absolute-magnitude range, that is, Sample D for both LCDM and SCDM models. The analytical prediction of the log-normal model (Eq. (13)) is also plotted with  $\sigma$  and  $\sigma_1$  calculated from the fitting formula of the power spectrum of the LCDM model by Peacock & Dodds (1996).

Figure 9 addresses three issues: first, the comparison between the log-normal model and the simulated MFs, which corresponds to the MFs for dark matter, second, the comparison between the simulated MFs and the observed MFs, and third, the comparison among the observed MFs of galaxy subsamples of different luminosity. First we find that the log-normal predictions agree well with the MFs for dark matter, even though the shape of the volume is wedge-like. This means that the observational effects on the MFs, such as the survey shape and the redshift distortion, are negligible, at least in the samples that we analyze. These results are consistent with previous results on the genus analysis for the SDSS Early Data Release (Hoyle et al. 2002; Hikage et al. 2002).

Next, we find that the observations agree better with the mock results of the LCDM model than with those for the SCDM model, for all of the MFs at all smoothing scales considered. Assuming a scale-invariant linear bias between dark matter and galaxies, the agreement is consistent with the  $\Lambda$ -dominated spatially-flat model with random-Gaussian initial conditions.

Finally, the luminosity dependence of the MFs is found to be small compared with the standard deviation. We plot the difference between the MFs of the observation and the mock samples (subtraction of the mock results from the observed MFs at each  $\nu$ ) in the right panels of Figure 9. We find that there is no clear difference between the MFs for galaxy samples with different luminosities. Our results suggest that the sensitivity of the nonlinearity of the biasing to the galaxy luminosity is small, in other words, the biasing effect of galaxy luminosity is negligible, at least on the volume-scale of ‘Sample 12’.

Figure 10 shows the MFs as a function of  $\nu_f$  defined from the volume fraction (Eq. [11]). Instead of the log-normal model prediction, the analytical predictions in random-Gaussian statistics are plotted. All of our results favor the LCDM model with random-Gaussian initial conditions.

### 4.4. Morphological Segregation

In this subsection we perform a quantitative analysis of the dependencies of the MFs on morphological type of galaxies (*cf.* Figure 6). Similar to the analysis of luminosity segregation

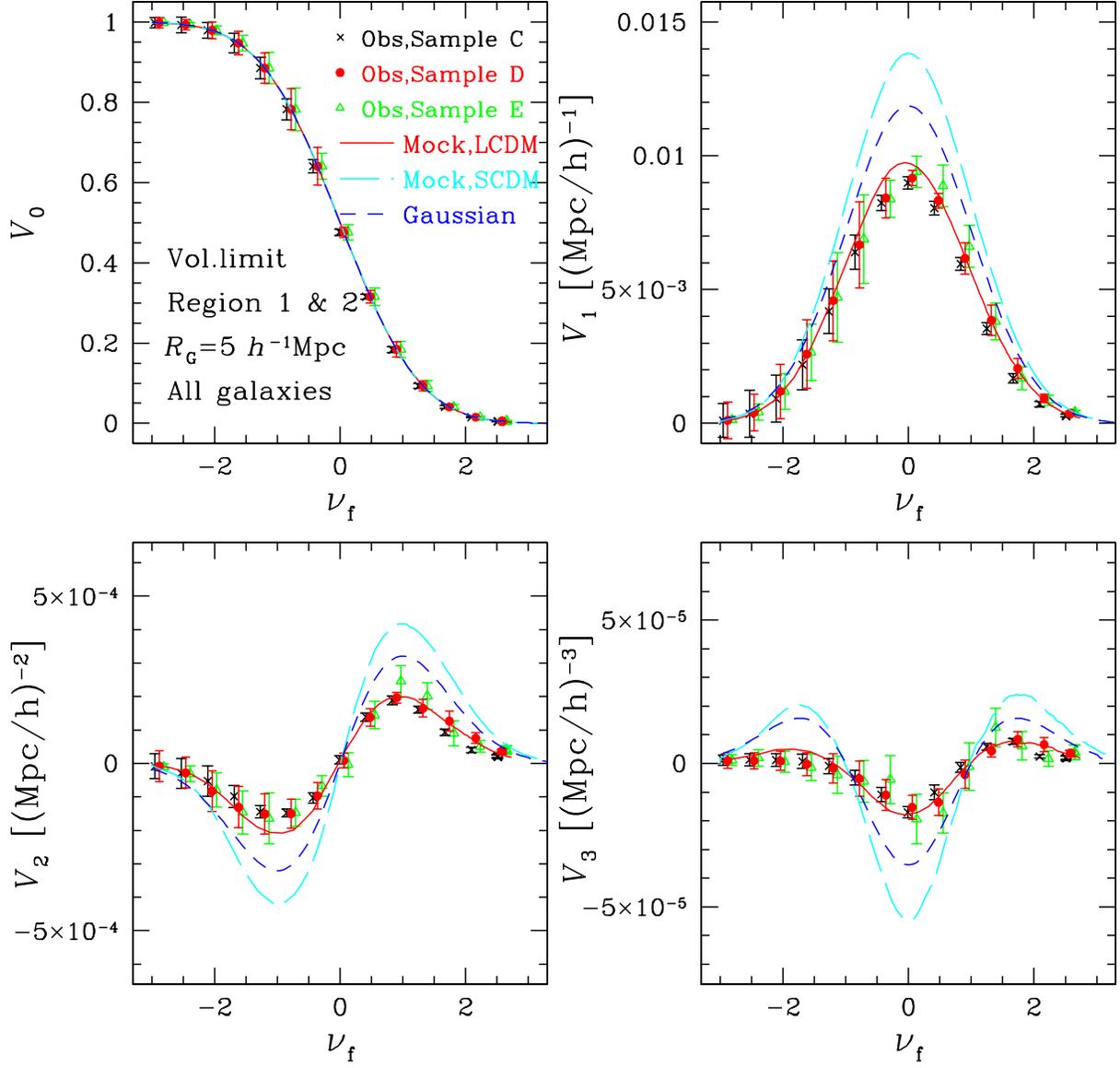


**Fig. 10.** MFs as a function of  $\nu_f$  for  $R_G = 5h^{-1}\text{Mpc}$  in Region 1 and Region 2 together. (Compare Figure 9 for the MFs as a function of  $\nu_\sigma$ ).

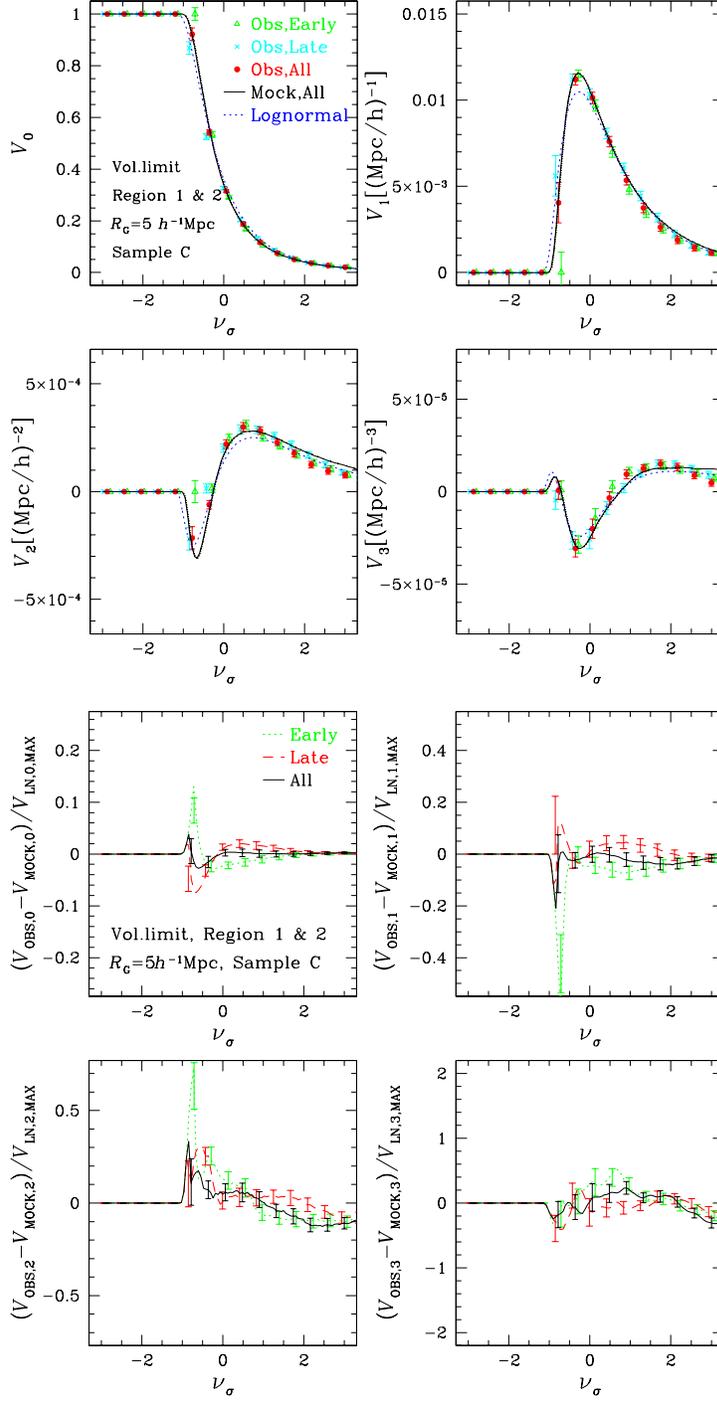


**Fig. 11.** Comparison of the MFs of a volume-limited sample C of Early-type galaxies (open triangles), Late-type galaxies (crosses) and All galaxies (filled circles). Plotted lines are the average between Region 1 and Region 2 smoothed at  $R_G = 5h^{-1}\text{Mpc}$ . The lower panel displays the difference between the observed and mock sample MFs, normalized by the amplitude of each MF predicted from the log-normal model. Sampling errors estimated from mock samples are plotted with the observational results. Averaged MFs of the mock samples for the distribution of all galaxies based on LCDM are plotted with solid lines. Log-normal model predictions are also plotted with short dashed lines.

in the previous subsection, we here compare the MFs for a volume-limited sample, Sample C, smoothed at  $5h^{-1}\text{Mpc}$  for different morphological types: Early-type, Late-type, and All galaxies shown in Figure 11. For comparison we plot the MFs for dark matter based on the LCDM and SCDM models, as well as the log-normal predictions.

In the lower panel of Figure 11, which shows the difference between the observed MFs and simulated MFs (the same as the lower panel of Figure 9), we find that the variations of the MFs for different galaxy type is small enough to conclude that morphological biasing of the MFs is negligible in ‘Sample 12’.

## 5. Summary and Discussion

We present results of a detailed morphometric analysis of a sample of SDSS galaxy data containing 154844 galaxies (‘Sample 12’) employing the complete set of Minkowski Functionals (MFs). To test for systematic errors in calculating the MFs of isodensity surfaces, we employ two complementary computational methods for the MFs: Crofton’s formula and Koenderink invariants. We find that these methods produce results that agree to within statistical errors, despite the complicated shape of the survey region. A possible exception to this agreement occurs for the most sensitive MF,  $V_2$ , but even in this case the dependence on method becomes small when the computed region is limited to several pixels inward from the survey edge. By constructing volume-limited samples, in which the distribution of galaxies in predefined magnitude ranges is homogeneous, we conduct a detailed analysis of the observed MFs for galaxies within different magnitude ranges and for galaxies of different morphological type. We compare these results with those estimated for the MFs of mock samples drawn from N-body simulations.

Let us summarize our results according to the three primary goals mentioned in Introduction.

1) Primordial Gaussianity: The good match between the observed MFs and the mock predictions based on the LCDM model with the initial random-Gaussianity might be interpreted to imply that the primordial Gaussianity is confirmed. A more conservative interpretation is that, given the size of the estimated uncertainties, these data do not provide evidence for initial non-Gaussianity, i.e., the data are *consistent* with primordial Gaussianity. Unfortunately due to the statistical limitation of current SDSS data, it is not easy to put more quantitative statement concerning the initial Gaussianity, but this is definitely what we intend to conduct with the improved datasets available in near future.

Moreover, in order to go further and place more quantitative constraints on primordial Gaussianity with upcoming data, one needs a more precise and reliable theoretical model for the MFs which properly describes the nonlinear gravitational effect possibly as well as galaxy biasing beyond the simple mapping on the basis of the volume fraction. A perturbative approach by Matsubara (1994) combined with an extensive simulation mock sample analysis may be a

promising strategy for this purpose.

2) Evolution of galaxy clustering: Galaxy biasing is another source of uncertainty for relating the observed MFs to those obtained from the mock samples for dark matter distributions (e.g. Hikage et al. 2001). If LCDM is the correct cosmological model, the good match of the MFs for mock samples from the LCDM simulations to the observed SDSS MFs may indicate that nonlinearity in the galaxy biasing is relatively small, at least small enough that it does not significantly affect the MFs (The MFs as a function of  $\nu_\sigma$  remain unchanged for the linear biasing). Furthermore, we show that the dependence of the nonlinearity of the biasing on the luminosity and the morphological type of galaxies is also very small. Our observational results that the effect of the galaxy biasing on the MFs is small is consistent with the predictions of theoretical studies (e.g. Benson et al. 2001).

3) Fair sample hypothesis: The observed morphological fluctuations inferred from the comparison of Region 1 and Region 2 of ‘Sample 12’ are indeed consistent with those exhibited in our mock catalogues.

Thus our overall conclusion is that the simulations of the LCDM model with primordial random–Gaussianity reproduce the observed MFs within the statistical errors. Differences between the MFs for the mock samples drawn from simulations of the LCDM and SCDM models arise mainly from their power spectra. The present MFs’ analysis places constraints on the cosmological models that are consistent with previous results using the two–point correlation function, but does not yet exploit the full advantage of the MFs as a complementary statistic to the conventional two–point correlation function, at least on the level of ‘Sample 12’.

While we found that the dependence of the MFs on the luminosity and the morphological type of galaxies is weak and both distributions are comparable within the statistical error, we believe that the systematic differences due to these galaxy properties (as suggested for the genus statistic by Hoyle et al. 2002) will certainly be detectable in the near future.

We thank Y. P. Jing for kindly providing us his N–body simulation data which were used in generating mock samples. T. B. acknowledges hospitality at the University of Tokyo and financial support by the Research Center for the Early Universe (RESCEU). I. K. gratefully acknowledges support from the Takenaka-Ikueikai fellowship. Numerical computations were carried out at ADAC (the Astronomical Data Analysis Center) of the National Astronomical Observatory, Japan (project ID: mys02). This research was also supported in part by the Grants–in–Aid from Monbu–Kagakusho and Japan Society of Promotion of Science (12640231, 13740150, 14102004, and 1470157), and by the Sonderforschungsbereich (SFB) 375 ‘Astroparticle physics’ of Deutsche Forschungsgemeinschaft (DFG). M.S.V. acknowledges the support of NSF grant AST 00-71201 and the John Templeton Foundation. J.R.G. was supported by NSF grant AST 99-00772.

Funding for the creation and distribution of the SDSS Archive has been provided by the

Alfred P. Sloan Foundation, the Participating Institutions, the National Aeronautics and Space Administration, the National Science Foundation, the U.S. Department of Energy, the Japanese Monbukagakusho, and the Max Planck Society. The SDSS Web site is <http://www.sdss.org/>.

The SDSS is managed by the Astrophysical Research Consortium (ARC) for the Participating Institutions. The Participating Institutions are The University of Chicago, Fermilab, the Institute for Advanced Study, the Japan Participation Group, The Johns Hopkins University, Los Alamos National Laboratory, the Max-Planck-Institute for Astronomy (MPIA), the Max-Planck-Institute for Astrophysics (MPA), New Mexico State University, University of Pittsburgh, Princeton University, the United States Naval Observatory, and the University of Washington.

## References

- Bardeen, J. M., Bond, J. R., Kaiser, N., & Szalay, A. S. 1986, *ApJ*, 304, 15
- Benson, A. J., Frenk, C. S., Baugh, C. M., Cole, S., & Lacey, C. G. 2001, *MNRAS*, 327, 1041
- Blanton, M. R., Lupton, R. H., Maley, F. M., Young, N., Zehavi, I., & Loveday, J. 2003, *AJ*, 125, 2276
- Colley, W., & Gott, J.R. 2003, *ApJ*, submitted. (astro-ph/0303020)
- Crofton, M. W. 1868, *Philos. Trans. R. Soc. London*, A, 158, 181
- Eisenstein, D. J., Annis, J., Gunn, J. E., Szalay, A. S., Connolly, A. J., Nichol, R. C., Bahcall, N. A., Bernardi, M., et al. 2001, *AJ*, 122, 2267
- Fukugita, M., Ichikawa, T., Gunn, J. E., Doi, M., Shimasaku, K., and Schneider, D. P. 1996, *AJ*, 111, 1748
- Gott, J. R., III, Melott, A. L., & Dickinson, M. 1986, *ApJ*, 306, 341
- Gott, J. R., III et al. 1989, *ApJ*, 340, 625
- Gunn, J. E., Carr, M., Rockosi, C., Sekiguchi, M., Berry, K., Elms, B., De Haas, E., Ivezić, Ž., et al. 1998, *AJ*, 116, 3040
- Hadwiger, H., *Vorlesungen über Inhalt, Oberfläche und Isoperimetrie*, Springer Verlag, Berlin, 1957
- Hikage, C., Taruya, A., & Suto, Y. 2001, *ApJ*, 556, 641
- Hikage, C., Suto, Y., Kayo, I, Taruya, A., Matsubara, T., Vogeley, M. S., Hoyle, F., Gott, J. R., III, Brinkmann, J., for the SDSS collaboration 2002, *PASJ*, 54, 707
- Hikage, C., Taruya, A., & Suto, Y. 2003, *PASJ*, 55, No2
- Hogg, D. W., Finkbeiner, D. P., Schlegel, D. J., & Gunn, J. E. 2001, *AJ*, 122, 2129
- Hoyle, F., et al. 2002, *ApJ*, 580, 663
- Jing, Y. P., & Suto, Y. 1998, *ApJ*, 494, L5
- Kerscher M., Schmalzing J., Buchert T., & Wagner H. 1997, In R. Bender, T. Buchert and P. Schneider, editors, *Proc. 2<sup>nd</sup> SFB workshop on Astro-particle physics, Ringberg 1996* (Report SFB375/P002, pp. 83–98, Ringberg, Tegernsee, 1996)
- Kerscher, M., Schmalzing, J., Buchert, T., & Wagner, H. 1998, *A&A*, 333, 1
- Kerscher, M. 2000, *Statistical Analysis of Large-scale Structure in the Universe*, Lecture Notes in

- Physics 554, 36, K.R. Mecke, D. Stoyan (Eds.): Statistical Physics and Spatial Statistics, The Art of Analyzing and Modeling Spatial Structures and Pattern Formation (Springer Heidelberg, 2000)
- Kerscher, M., Mecke, K.-R., Schmalzing, J., Beisbart, C., Buchert, T., & Wagner, H. 2001, A&A, 373, 1
- Koenderink, J. J. 1984, Biol. Cybern., 50, 363
- Komatsu, E., et al. 2003, ApJ, in press (astro-ph/0302223)
- Matsubara, T. 1994, ApJ, 434, L43
- Matsubara, T., & Yokoyama, J. 1996, ApJ, 463, 409
- Mecke, K. R., Buchert, T. & Wagner, H. 1994, A&A, 288, 697
- Melott, A. L. 1988, in: Proceedings of the Lawrence Workshop on Cosmological Topology, April 26-29, 1988, San Francisco: Astronomical Society of the Pacific (ASP), 1988, ed. by Melott, A. L.
- Peacock, J. A., & Dodds, S. J. 1996, MNRAS, 280, L19
- Pier, J., Munn, J. A., Hindsley, R. B., Hennessy, G. S., Kent, S. M., Lupton, R. H., Ivezić, Ž., for the SDSS collaboration 2003, AJ, 125, 1559
- Rhoads, J. E., Gott, J. R., III, & Postman, M. 1994, ApJ, 421, 1
- Ryden, B. 1988, ApJ, 333, L41
- Ryden, B. S., et al. 1989, ApJ, 340, 647
- Sahni, V., Sathyaprakash, B.S., Shandarin, S.F. 1998, ApJ, 495, L5
- Schneider, R., Curvature measures of convex bodies, Ann. Math. pura appl., 1978, 116, 101
- Schlegel, D. J., Finkbeiner, D. P., & Davis, M. 1998, ApJ, 500, 525
- Schmalzing, J., & Buchert, T. 1997, ApJ, 482, L1
- Schmalzing J., Buchert T., Melott A.-L., Sahni V., Sathyaprakash B.S., & Shandarin S.F. 1999a, ApJ, 526, 568
- Schmalzing, J., Gottlöber, S., Kravtsov, A., & Klypin, A. 1999b, MNRAS, 309, 1007
- Sheth, J. V., Sahni, V., Shandarin, S. F., & Sathyaprakash, B. S. 2003, MNRAS, accepted, (astro-ph 0210136)
- Shimasaku, K. et al. 2001, AJ, 122, 1238
- Smith, J. A., Tucker, D. L., Kent, S., Richmond, M. W., Fukugita, M., Ichikawa, T., Ichikawa, S., Jorgensen, A. M., et al. 2002, AJ, 123, 2121
- Spiegel, D. N. et al. 2003, ApJ, in press (astro-ph/0302209)
- Stoughton, C., Lupton, R. M., Bernardi, M., Blanton, M. R., Burles, S., Castander, F. J., Connolly, A. J., Eisenstein, D. J., et al. 2002, AJ, 123, 485
- Strauss, M. A., Weinberg, D. H., Lupton, R. M., Narayanan, V., Annis, J., Bernardi, M., Blanton, M. R., Burles, S., et al. 2002, AJ, 124, 1810
- Tomita, H., Statistics and geometry of random interface systems, in: Formation, dynamics and statistics of patterns (Kawasaki, K., Suzuki, M., & Onuki, A., eds.), Vol.1, World Scientific, 1990, 113
- Vogeley, M. S., Park, C., Geller, M. J., Huchra, J. P., & Gott, J. R., III 1994, ApJ, 420, 525
- Weinberg, D. H. 1988, PASP, 100, 1373
- York, D. G., Adelman, J., Anderson, J. E., Jr., Anderson, S. F., Annis, J., Bahcall, N. A., Bakken, J. A., Barkhouser, R., et al. 2000, AJ, 120, 1579.

## Appendix A: Calculating higher-order Minkowski Functionals from the Koenderink invariants of a scalar field

As stated in the main text, the higher-order Minkowski Functionals  $V_\mu$ ,  $\mu = 1, \dots, d$  of any pattern  $P \subset \Omega$  in  $d$  dimensions can be calculated by integrating the partial Minkowski Functionals  $v_\mu(\mathbf{x})$  along the surface of the pattern  $\partial P$ :

$$V_\mu = \int_{\partial P} d^{d-1}S v_\mu(\mathbf{x}), \quad (18)$$

where  $d^{d-1}S$  is the  $d-1$ -dimensional surface element at  $\mathbf{x}$ . Unfortunately, this formula is of little practical use for evaluating the Minkowski Functionals of a pattern  $P_\nu$  given as the isocontour of a scalar field  $u(\mathbf{x})$ , that is

$$P_\nu = \{\mathbf{x} | u(\mathbf{x}) \geq \nu\}. \quad (19)$$

We aim to convert the surface integrals above into volume integrals of functions of the field and its derivatives.

It is relatively simple to convert the surface integral itself; we have

$$\int_{\partial P_\nu} d^{d-1}S = \int_{\Omega} d^d x |\nabla u(\mathbf{x})| \delta(u(\mathbf{x}) - \nu), \quad (20)$$

where  $\nabla u(\mathbf{x})$  is the gradient of the field and  $\delta(u(\mathbf{x}) - \nu)$  is a Dirac  $\delta$ -function selecting only the surface of the pattern from the whole support  $\Omega$ .

As far as the local Minkowski Functionals  $v_\mu(\mathbf{x})$  are concerned, we will restrict ourselves to the relevant case of three dimensions. Then, the local Minkowski Functionals are proportional to the mean and Gaussian curvatures,  $H$  and  $G$ , of the surface:

$$v_1(\mathbf{x}) = \frac{1}{6} \quad (21)$$

$$v_2(\mathbf{x}) = \frac{1}{3\pi} H \quad (22)$$

$$v_3(\mathbf{x}) = \frac{1}{4\pi} G. \quad (23)$$

In order to express the curvatures in terms of derivatives, we perform some textbook differential geometry. The surface around a point  $\mathbf{x}$  can be parameterized locally with two parameters  $t_a$ ,  $a = 1, 2$ . The isocontour of the field  $u(\mathbf{x})$  at threshold  $\nu$  is characterized by a simple implicit equation:

$$\nu = u(\mathbf{x}). \quad (24)$$

Taking the derivative of this equation with respect to the surface parameters  $t_a$  yields a system of equations that allows us to determine the fundamental forms of the iso-surface. We have<sup>1</sup>:

---

<sup>1</sup> In the following, ordinary partial derivatives with respect to a coordinate in three dimensions are denoted by the index of the coordinate following a comma, while derivatives along the surface are denoted with the index of the surface parameter following a semicolon. Indices named  $a$  and  $b$  are used for the surface

$$0 = u_{;a} = u_{;i}x_{i;a}, \quad \text{and} \quad 0 = u_{;ab} = u_{;ij}x_{i;a}x_{j;b} + u_{;i}x_{i;ab}. \quad (25)$$

The first part of the system,

$$0 = u_{;i}x_{i;a}, \quad (26)$$

can be solved to yield the tangent vectors  $\mathbf{x}_{;a}$ ,  $a = 1, 2$  of the surface. We will use<sup>2</sup>

$$x_{i;a} = \varepsilon_{aij}u_{;j}. \quad (27)$$

The scalar products of the tangent vectors form the entries of the first fundamental form of the surface, the metric tensor  $g_{ab}$ . We have

$$g_{ab} = x_{i;a}x_{i;b} = \delta_{ab}u_{;i}u_{;i} - u_{;a}u_{;b}. \quad (28)$$

In the following, we need the determinant  $g$  of the metric tensor, given as

$$g = \det g_{ab} = u_{;3}^2 u_{;i}u_{;i} \quad (29)$$

and its inverse

$$g^{ab} = \frac{\delta_{ab}u_{;3}^2 + u_{;a}u_{;b}}{g}. \quad (30)$$

In order to obtain the second fundamental form of the surface, we need the second derivatives  $x_{i;ab}$  of the surface and the components  $n_i$  of the normal vector. Equation (25) yields the condition

$$u_{;i}x_{i;ab} = -u_{;ij}x_{i;a}x_{j;b} \quad (31)$$

for the second derivatives, which will turn out to be enough for our purposes. The normal vector is proportional to the gradient, and has to be normalized of course, so we choose

$$n_i = -\frac{u_{;i}}{(u_{;j}u_{;j})^{1/2}}. \quad (32)$$

The minus sign directs the normal vector towards regions of lower density; this corresponds to the intuitive expectation that the maxima of the field should be surrounded by islands of isocontour. Finally, we obtain the pseudo-tensor  $b_{ab}$ , containing the components of the second fundamental form of the surface

$$b_{ab} = -n_i x_{i;ab} = \frac{u_{;i}\varepsilon_{aij}u_{;jk}\varepsilon_{bkl}u_{;l}}{(u_{;m}u_{;m})^{1/2}}. \quad (33)$$

Again, we need the determinant  $b$  of this object. Some algebra leads to the result

$$b = \det b_{\mu\nu} = u_{;3}^2 \frac{\varepsilon_{ijk}\varepsilon_{lmn}u_{;i}u_{;l}u_{;jm}u_{;kn}}{u_{;o}u_{;o}^{1/2}}. \quad (34)$$

---

parameters and therefore run over 1, 2, while indices named  $i, j, \dots$  run from 1 to 3. Summation over indices occurring in pairs is understood.

<sup>2</sup> In fact, this solution is not unique, reflecting the freedom of parameterization. However, as long as the tangent vectors are not colinear, the final results, namely the local Minkowski Functionals, are independent of the parameterization.

With these preparations, the mean curvature  $H$  and the Gaussian curvature  $G$  of the isocontour of a scalar field can be expressed in terms of the field's derivatives. In terms of the components of the first and second fundamental form, they are given as

$$H = \frac{1}{2}g^{\mu\nu}b_{\mu\nu}, \quad G = \frac{b}{g}. \quad (35)$$

Putting the results from above into these formulae yields

$$H = \frac{\varepsilon_{ijk}\varepsilon_{ilm}u_{,j}u_{,l}u_{,km}}{2(u_{,n}u_{,n})^{3/2}}, \quad (36)$$

$$G = \frac{\varepsilon_{ijk}\varepsilon_{lmn}u_{,i}u_{,l}u_{,jm}u_{,kn}}{(u_{,o}u_{,o})^2}. \quad (37)$$

## Appendix B: Analysis of Magnitude-limited Samples

As discussed above, in this paper we focus on the analysis of volume-limited samples to avoid the systematic effects of variation with redshift of the mean galaxy density and range of galaxy luminosity. However, the statistical error of the MFs becomes large in volume-limited samples due to the small number density or the small volumes of such samples. In apparent-magnitude limited samples we can make use of nearly all of the data. Our results for volume-limited samples suggest that the luminosity bias is small and, therefore, that it might be reasonable to analyze apparent-magnitude limited samples. To do so requires correction for the variation with redshift in the expected galaxy density.

We compute the selection function  $\phi(z)$ , by integrating over the Schechter form of the luminosity function,

$$\phi(z) \propto \int_{M_{\min}(z)}^{M_{\max}(z)} \phi_* [10^{0.4(M_*-M)}]^{\alpha+1} \times \exp[-10^{0.4(M_*-M)}] dM, \quad (38)$$

with parameters for all galaxies measured in the  $^{0.1}r$  band by Blanton et al. (2002) and those for Early- and Late-type galaxies measured in the  $r$ -band by Nakamura et al (listed in Table 5). Note that the  $^{0.1}r$  band corresponds to the  $r$ -band shifted to match their rest-frame shape at  $z = 0.1$ . The limits of integration are the absolute-magnitude limits.

$$M_{\max/\min}(z) = m_{\max/\min} - 5 \log \left[ \frac{(1+z)d_c(z)}{10 \text{pc}} \right] - K(z). \quad (39)$$

We use apparent-magnitude limits  $m_{\max} = 17.5$ ,  $m_{\min} = 14.5$ , and apply an approximate K-correction factor  $K(z) = 0.9z$  ( $K(z) = 0.9(z - 0.1)$  for  $^{0.1}r$  band). Figure 5 shows the number density distributions of our samples of All, Early-type and Late-type galaxies (histograms) compared with fits from Equation (38) for both Region 1 and Region 2. We list the properties of the magnitude-limited samples with absolute-magnitude range from  $-23$  to  $-17$  in Table 6. The redshift range for each sample is determined to be the region where the mean separation

**Table 5.** Parameter values of the Schechter form of the luminosity function (Eq.(38)) for All, Early-type, and Late-type galaxies, where the  $^{0.1}r$ -band corresponds to the  $r$ -band shifted to match their rest-frame shape at  $z = 0.1$ .

galaxy type	band	$M_* - 5\log_{10}h$	$\alpha$	$\phi_*(10^{-2}(h^{-1}\text{Mpc})^{-3})$
All	$^{0.1}r$	-20.44	-1.05	1.49
Early-type	$r$	-20.62	-0.68	0.67
Late-type	$r$	-20.35	-1.12	1.09

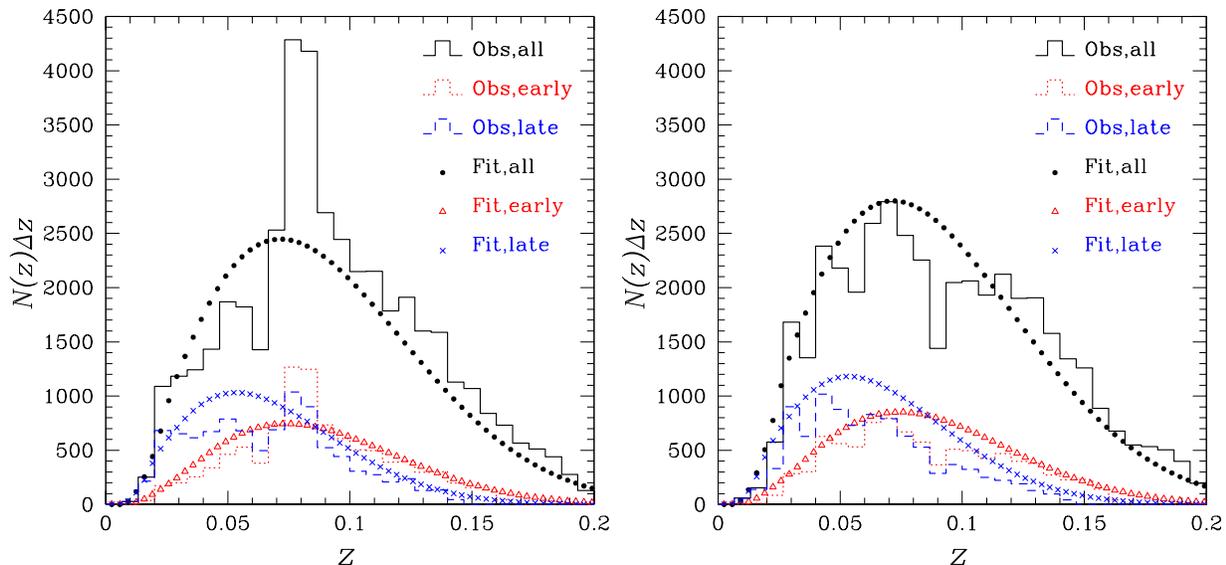


**Fig. 12.** Number density distribution of our SDSS galaxy sample for All (solid histogram), Early-type (dotted histogram), and Late-type galaxies (dashed histogram) in Region 1 and Region 2, respectively. The estimations with the Schechter form of the luminosity function (Eq. (38)) fitted to the observation are also plotted for All (filled circles), Early-type (open triangles) and Late-type (crosses) galaxies. The redshift width ( $\Delta z$ ) of the histogram is  $1/150$ .

of galaxies,  $\phi(z)^{-1/3}$ , is smaller than the smoothing scale. To construct mock samples with the same redshift distribution, we randomly select dark matter particles in the wedge samples in real space according to the selection function to reproduce the number of observed SDSS galaxies in the current samples. To correct the galaxy density field for the variation with distance of the selection function, we weight each galaxy by the inverse of the selection function  $\phi(z)^{-1}$  in redshift space (e.g., Rhoads et al. 1994; Vogeley et al. 1994). Table 7 lists  $N_{\text{res}}$  (Eq. (17)) and  $\sigma$  of galaxies in each sample and  $\sigma$  with one-sigma error estimated from the mock samples. For all of the smoothing lengths the table shows the general feature that clustering is strong for Early-type galaxies, and weak for Late-type galaxies.

Figure 5 shows the comparison of MFs for All, Early-type and Late-type galaxies with error bars estimated from mock samples for each type of galaxies. The averaged MFs of mock samples for all galaxies in the LCDM model and the log-normal predictions are also

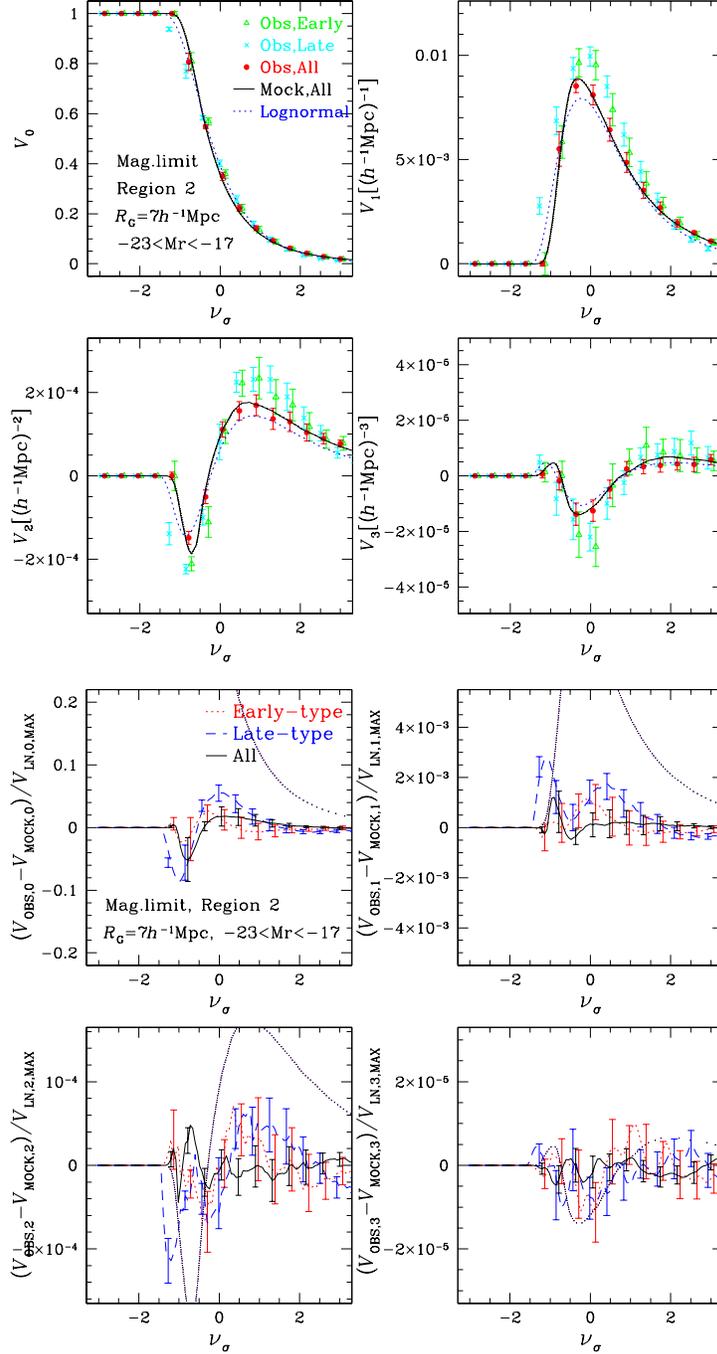


**Fig. 13.** *Upper:* Comparison of the MFs between the magnitude-limited samples for All (filled circles), Early-type (open triangles) and Late-type galaxies (crosses). Error bars, estimated from the mock results, are added to the observational results. The averaged MFs from mock samples for all galaxies are also plotted with solid lines. The log-normal model predictions (Eq. (13)) are plotted with dotted lines. *Lower:* Dependency of the galaxy type on the MFs for magnitude-limited samples of SDSS galaxies. Subtractions of the MFs at each  $\nu_\sigma$  of the mock results from the observed MFs are plotted for Early-type (dotted lines), Late-type (dashed lines) and All (solid lines) galaxies with error bars estimated from the mock results. We adopt the smoothing scale of  $R_G = 7h^{-1} \text{Mpc}$  and the data of Region 2.

**Table 6.** Properties of each magnitude-limited sample of SDSS galaxies including the galaxy type, the smoothing scale  $R_G$ , the redshift range, the number of SDSS galaxies in each sample  $N_{\text{gal}}$ , and the mean number of mass particles in six mock samples  $N_{\text{particle}}$ .

type	$R_G$	redshift range	$N_{\text{gal}}$		$N_{\text{particle}}$	
			Region1	Region2	Region1	Region2
All	$5h^{-1}\text{Mpc}$	$0.009 < z < 0.088$	21898	20768	18325	21454
All	$7h^{-1}\text{Mpc}$	$0.008 < z < 0.121$	32714	30231	29243	32950
All	$10h^{-1}\text{Mpc}$	$0.007 < z < 0.150$	39416	37512	34803	39689
All	$20h^{-1}\text{Mpc}$	$0.006 < z < 0.197$	43355	41805	38171	42050
Early	$7h^{-1}\text{Mpc}$	$0.013 < z < 0.082$	4657	4765	4672	5309
Early	$10h^{-1}\text{Mpc}$	$0.009 < z < 0.117$	8069	7146	8059	9232
Early	$20h^{-1}\text{Mpc}$	$0.007 < z < 0.167$	9889	9168	10153	11157
Late	$5h^{-1}\text{Mpc}$	$0.011 < z < 0.049$	4158	4390	4555	5532
Late	$7h^{-1}\text{Mpc}$	$0.008 < z < 0.078$	7003	7199	8262	9038
Late	$10h^{-1}\text{Mpc}$	$0.007 < z < 0.104$	8734	8444	10415	11852
Late	$20h^{-1}\text{Mpc}$	$0.006 < z < 0.145$	9761	9372	11891	13077

plotted. Focusing on the difference in morphological properties of the distribution due to the morphological type of galaxies, we plot the subtraction of the simulated results from the observed MFs for each type of galaxies, normalized by the MFs predicted from the log-normal model, in the lower panel of Figure 5. We conclude that also in the magnitude-limited samples the difference due to morphological type of galaxies cannot be appreciated, as was found for the volume-limited samples.

**Table 7.** Properties of the smoothed density field of each magnitude-limited sample including  $R_G$ , the mesh size of the simulation box, the galaxy type,  $N_{\text{res}}$  (Eq. (17)), the r.m.s. fluctuation  $\sigma$  of the SDSS galaxy number density field, and the averaged  $\sigma$  with one-sigma error of the particle number density field in the mock samples.

$R_G$ (mesh size)	type	$N_{\text{res}}$ (volume fraction)		$\sigma$ of SDSS galaxies		$\sigma$ of mock samples	
		Region1	Region2	Region1	Region2	Region1	Region2
$5h^{-1}\text{Mpc}$	All	464(0.71)	486(0.65)	1.17	0.97	$1.07 \pm 0.13$	$0.97 \pm 0.10$
$(2.1h^{-1}\text{Mpc})$	Late	112(0.59)	112(0.52)	0.86	0.74	$0.99 \pm 0.12$	$0.94 \pm 0.19$
$7h^{-1}\text{Mpc}$	All	424(0.70)	441(0.64)	0.86	0.88	$0.83 \pm 0.09$	$0.80 \pm 0.07$
$(2.9h^{-1}\text{Mpc})$	Early	113(0.59)	114(0.52)	0.98	0.74	$0.84 \pm 0.12$	$0.80 \pm 0.10$
	Late	121(0.59)	122(0.52)	0.66	0.64	$0.86 \pm 0.14$	$0.81 \pm 0.11$
$10h^{-1}\text{Mpc}$	All	182(0.46)	177(0.39)	0.63	0.64	$0.66 \pm 0.05$	$0.66 \pm 0.04$
$(3.8h^{-1}\text{Mpc})$	Early	65(0.36)	62(0.30)	0.73	0.72	$0.63 \pm 0.07$	$0.59 \pm 0.05$
	Late	48(0.33)	45(0.27)	0.66	0.55	$0.59 \pm 0.07$	$0.59 \pm 0.06$
$20h^{-1}\text{Mpc}$	All	29(0.27)	26(0.21)	0.34	0.45	$0.33 \pm 0.05$	$0.35 \pm 0.04$
$(5.3h^{-1}\text{Mpc})$	Early	12(0.20)	10(0.14)	0.34	0.43	$0.32 \pm 0.07$	$0.31 \pm 0.06$
	Late	7(0.15)	5(0.11)	0.28	0.30	$0.31 \pm 0.07$	$0.32 \pm 0.07$

This figure "f1a.jpg" is available in "jpg" format from:

<http://arxiv.org/ps/astro-ph/0304455v3>

This figure "f1b.jpg" is available in "jpg" format from:

<http://arxiv.org/ps/astro-ph/0304455v3>

This figure "f2a.jpg" is available in "jpg" format from:

<http://arxiv.org/ps/astro-ph/0304455v3>

This figure "f2b.jpg" is available in "jpg" format from:

<http://arxiv.org/ps/astro-ph/0304455v3>

This figure "f2c.jpg" is available in "jpg" format from:

<http://arxiv.org/ps/astro-ph/0304455v3>

This figure "f3a.jpg" is available in "jpg" format from:

<http://arxiv.org/ps/astro-ph/0304455v3>

This figure "f3b.jpg" is available in "jpg" format from:

<http://arxiv.org/ps/astro-ph/0304455v3>

This figure "f3c.jpg" is available in "jpg" format from:

<http://arxiv.org/ps/astro-ph/0304455v3>

This figure "f6a.jpg" is available in "jpg" format from:

<http://arxiv.org/ps/astro-ph/0304455v3>

This figure "f6b.jpg" is available in "jpg" format from:

<http://arxiv.org/ps/astro-ph/0304455v3>

This figure "f6c.jpg" is available in "jpg" format from:

<http://arxiv.org/ps/astro-ph/0304455v3>

This figure "f6d.jpg" is available in "jpg" format from:

<http://arxiv.org/ps/astro-ph/0304455v3>